The Journal of Chemical Physics

RESEARCH ARTICLE | FEBRUARY 03 2026

Improved molecular conductance predictions using wavefunction-in-DFT quantum embedding

Dávid P. Jelenfi ; Dávid Mester ; Attila Tajti ; Péter G. Szalay

J. Chem. Phys. 164, 054105 (2026)
https://doi.org/10.1063/5.0313307

AIP Publishing

The Journal of Chemical Physics ARTICLE pubs.aip.org/aip/jcp

Improved molecular conductance predictions using wavefunction-in-DFT quantum embedding

Cite as: J. Chem. Phys. 164, 054105 (2026); doi: 10.1063/5.0313307
Submitted: 21 November 2025 • Accepted: 13 January 2026 •
Published Online: 3 February 2026

Dávid P. Jelenfi,[1,2] Dávid Mester,[3] Attila Tajti,[2,a)] and Péter G. Szalay[2]

AFFILIATIONS

[1] Hevesy György Ph.D. School of Chemistry, ELTE Eötvös Loránd University, Pázmány Péter Sétány 1/A, Budapest H-1117, Hungary
[2] Laboratory of Theoretical Chemistry, Institute of Chemistry, ELTE Eötvös Loránd University, Pázmány Péter Sétány 1/A, Budapest H-1117, Hungary
[3] Department of Physical Chemistry and Materials Science, Faculty of Chemical Technology and Biotechnology, Budapest University of Technology and Economics, Műegyetem rkp. 3, H-1111 Budapest, Hungary

[a)] **Author to whom correspondence should be addressed:** attila.tajti@ttk.elte.hu

ABSTRACT

A novel electronic structure methodology to describe electron transport in single-molecule junctions (SMJs) within non-equilibrium Green's function theory is presented. The approach is based on a formally exact, projection-based quantum embedding technique that combines correlated many-electron wavefunction models for the molecular region with a density functional theory (DFT) description of the metallic electrodes. This is achieved by constructing a specialized Hamiltonian for the molecular domain, leveraging Dyson orbitals corresponding to the ionized and electron-attached states of the embedded molecule. The effectiveness of this wavefunction-in-DFT embedding scheme is demonstrated through transport calculations for SMJs containing benzene-1,4-diamine and its substituted derivatives, employing Hartree–Fock, SOS-ADC(2), and CCSD methods for the molecular subsystem. The results show a marked improvement in the predicted zero-bias conductance compared to conventional DFT-based transport modeling employing the PBE functional. The proposed methodology provides a systematic way to select the most suitable electronic structure methods for the different parts of the system, maintaining a balance between accuracy and computational cost, while ensuring a proper description of electronic correlation within the molecule, which may notably impact electron transport in certain systems.

I. INTRODUCTION

Single-molecule junctions (SMJs), consisting of a single molecule connected to metallic nanoscale leads, provide a fundamental platform for investigating charge transport through molecular systems. Understanding these phenomena continues to attract significant attention across various fields, including material science and biochemistry. The key measurable quantity in these systems is the zero-bias conductance, which is primarily determined by the alignment of the energy levels of the molecule relative to the Fermi level of the metallic leads.[1,2]

In theoretical studies, the conductance is typically evaluated using the non-equilibrium Green's function (NEGF) formalism combined with a mean-field electronic structure method. In most cases, density-functional theory (DFT) is employed due to its convenience and balance between accuracy and computational cost.[3,4] However, standard functionals such as the Perdew–Burke–Ernzerhof (PBE)[5] parametrization of the GGA functional, although well suited for metallic systems, often provide a qualitatively incorrect description of the molecular frontier orbital energies. PBE was several times found to significantly overestimate the energy of the highest occupied molecular orbital (HOMO) and underestimate that of the lowest unoccupied molecular orbital (LUMO), resulting in a systematic overestimation of the zero-bias conductance.[6–8] In our recent study,[8] we proposed an embedding framework that addresses this issue by treating the molecule and the metallic leads with distinct DFT functionals chosen according to their respective electronic characteristics. This DFT-in-DFT embedding approach outperformed the conventional NEGF-DFT model employing a single PBE functional. The main advantage of this scheme arises from the ability to select a separate functional for the molecule that predicts its energy levels with satisfying accuracy, while maintaining the computational efficiency of the method. Suitable functionals could be identified by benchmarking the accuracy

of the ionization potential (IP) and electron affinity (EA) values they provide for the isolated molecule. It was demonstrated that the use of different functionals for the molecule and the electrodes allows a more balanced description of both parts without any empirical adjustment or system-specific tuning. The accuracy of molecular energy levels can be further improved by using wavefunction theory (WFT) methods, which provide a proper, first-principles treatment of electron correlation, and several models are known to predict IP and EA values with high reliability. In this study, we extend our previous DFT-in-DFT embedding framework to a wavefunction-in-DFT (WFT-in-DFT) scheme, where the molecular region is treated at a correlated WFT level and the metallic environment is described by DFT. This extension retains the same embedding formulation based on the Huzinaga equation,[9] which enables an exact subsystem separation and the consistent coupling of regions described by different electronic structure methods.

We assess the performance of the new WFT-in-DFT embedding approach with the same test set as in our previous study,[8] including the benzene-1,4-diamine (BDA) molecule and its 2,3,5,6-tetramethyl- and 2,3,5,6-tetrafluoro-substituted variants (denoted as Me_4-BDA and F_4-BDA, respectively). These molecules serve as well-established benchmarks in single-molecule transport studies due to their well-characterized experimental conductances.[10–12] To evaluate the accuracy of the molecular description within the embedding framework, we compute and analyze the IP and EA values at different levels of theory, including the coupled-cluster singles and doubles (CCSD) and the scaled opposite-spin second order algebraic-diagrammatic construction [SOS-ADC(2)] methods, for both isolated and embedded molecules.

II. METHODOLOGY

We begin the presentation of the proposed methodology by briefly summarizing the key aspects of the transport calculations and the embedding scheme in Secs. II A and II B, whereas the main developments specific to the WFT-in-DFT formulation are discussed in detail in Secs. II C and II D.

A. Transmission calculation

The zero-bias conductance, which is the main quantity investigated experimentally, can be obtained from the Landauer formula,[13]

$$\mathscr{G} = \mathscr{G}_0\, T(E_F, V = 0), \tag{1}$$

where $\mathscr{G}_0 = 2e^2/h$ is the quantum of conductance and $T(E_F, V = 0)$ denotes the value of the *transmission function* at the Fermi level, E_F, corresponding to zero applied bias, V. The transmission function is the key quantity determined in theoretical approaches, as it describes the probability of electron transport through the system. For this purpose, the most widely used approach is the non-equilibrium Green's function (NEGF) theory.[4,14] Within this framework, the SMJ is modeled as an extended molecule (EM), which consists of the investigated molecule and two metallic electrodes, connected to semi-infinite metallic leads that serve as electron reservoirs representing the external circuit. According to the Meir–Wingreen formula,[15] the transmission function can be calculated from the Green's function of the EM as follows:

$$T(E, V) = \mathrm{Tr}\left[\mathbf{G}^r(E, V)\, \mathbf{\Gamma}_L(E, V)\, \mathbf{G}^a(E, V)\, \mathbf{\Gamma}_R(E, V)\right], \tag{2}$$

where $\mathbf{G}^{r/a}$ are the retarded and advanced Green's function matrices of the EM, and $\mathbf{\Gamma}_{L/R}$ denote the coupling matrices of the leads. In general, the Green's function matrix in the atomic orbital (AO) basis is evaluated as follows:

$$\mathbf{G}^r(E, V) = \left[(E + i\eta)\mathbf{S}_{EM} - \mathbf{H}_{EM} - \mathbf{\Sigma}_L(E, V) - \mathbf{\Sigma}_R(E, V)\right]^{-1}, \tag{3}$$

where $\mathbf{H}_{EM}$ and $\mathbf{S}_{EM}$ are the Hamiltonian and overlap matrices of the EM, and $\mathbf{\Sigma}_{L/R}$ represent the self-energies of the left and right leads. The latter are also used to determine the coupling matrices. In the NEGF-DFT framework, $\mathbf{H}_{EM}$ corresponds to the Kohn–Sham Hamiltonian obtained from a DFT calculation for the isolated EM, while the self-energies are derived from the periodic Kohn–Sham Hamiltonians of the leads, determined in separate periodic calculations for the lead(s) using the same DFT functional. A more detailed description of the NEGF formalism, the construction of the lead self-energies, and the practical aspects of the transmission calculations can be found in our previous work[8] and in Refs. 3, 4, 14, 16, and 17.

B. Huzinaga embedding approach

The use of different methods in the molecular and electrode regions of the extended molecule (EM) can be realized with the projection-based embedding (PbE) approach of Hégely and coworkers,[9] which is founded on the Huzinaga equation.[18] The procedure has been presented in detail in our recent study,[8] we only reiterate the key points of this concept here. In the PbE framework, the supersystem—corresponding to the EM in the present case—is partitioned into an active subsystem (the molecule, M) and an environment (the electrodes, El). An initial self-consistent field (SCF) calculation is first performed for the entire supersystem with a mean-field method that is suited for the environment. A natural choice for the latter is, in our case, DFT with a functional appropriate to describe the electrodes ($\mathbf{L}^{\mathrm{I}}$), for example, PBE.[5] The resulting Kohn–Sham molecular orbitals (MOs), which are eigenvectors of the Fock matrix $\mathbf{F}_{EM}$, are then localized using an appropriate algorithm to divide the supersystem density into molecular (M) and electrode (El) domains. Subsequently, the orbitals of the M domain are reoptimized with the so-called high-level functional $\mathbf{L}^{\mathrm{II}}$, in such a way that the space (and thus, the density) of the El domain is kept frozen and the orthogonality of the M and El subspaces is retained.

This procedure produces the embedded Fock matrix,

$$\tilde{\mathbf{F}}_{EM} = \mathbf{h}_M + \mathbf{L}^{\mathrm{II}}[\tilde{\mathbf{D}}_M] + \underbrace{\mathbf{h}_{El} + \left(\mathbf{L}^{\mathrm{I}}[\mathbf{D}_{EM}] - \mathbf{L}^{\mathrm{I}}[\mathbf{D}_M]\right)}_{\mathbf{v}_{\mathrm{emb.}}}, \tag{4}$$

where the last three terms, including the core Hamiltonian $\mathbf{h}_{El}$ and the two-electron contribution of the electrodes—expressed as the difference $(\mathbf{L}^{\mathrm{I}}[\mathbf{D}_{EM}] - \mathbf{L}^{\mathrm{I}}[\mathbf{D}_M])$—define the so-called *embedding potential* $\mathbf{v}_{\mathrm{emb.}}$, with $\mathbf{D}_P$ being the respective one-particle density matrices. The first two terms correspond to the molecule, with $\mathbf{h}_M$ being its core Hamiltonian and $\mathbf{L}^{\mathrm{II}}[\tilde{\mathbf{D}}_M]$ being the two-electron contribution, evaluated using $\mathbf{L}^{\mathrm{II}}$. In DFT-in-DFT embedding, this is the functional assigned to the active domain (functional II), whereas in WFT-in-DFT embedding, the Hartree–Fock (HF) method is used.

The orbitals generated in this step (i.e., the eigenvectors of $\tilde{\mathbf{F}}_{EM}$) are hereafter referred to as Huzinaga orbitals (HOs), with $\tilde{\mathbf{C}}$ being

the corresponding HO coefficient matrix. These are applied in a subsequent WFT step to compute the ionic many-electron states of the embedded molecule. While the actual localization scheme applied for separating the two subsystems was not found to affect the DFT-in-DFT results to a notable extent,[8] it is expected to be much more important when a WFT method is employed. The commonly used choice for localization is the subsystem projected atomic orbital decomposition (SPADE),[19] which performs well for the occupied space but often leads to a nonphysical behavior when applied to the virtual space.[20,21] Therefore, the projected atomic orbitals (PAOs)[22] were recommended in recent studies[21,23] to obtain the virtual space in WFT-in-DFT calculations involving correlated wave function models.

C. Dyson orbitals

One way to capture many-body effects in a molecular orbital picture is using Dyson orbitals (DOs),[24,25] that are one-electron functions emerging from the overlap of the neutral and ionic many-electron wave functions,

$$\phi_x^{\mathrm{I}}(\boldsymbol{r}_h) = \sqrt{n}\int {}^{n-1}\Psi_x(\boldsymbol{r}_2,\ldots,\boldsymbol{r}_n)\ {}^{n}\Psi_0(\boldsymbol{r}_h,\boldsymbol{r}_2,\ldots,\boldsymbol{r}_n)\,\mathrm{d}\boldsymbol{r}_2\ldots\mathrm{d}\boldsymbol{r}_n, \tag{5}$$

$$\phi_x^{\mathrm{E}}(\boldsymbol{r}_e) = \sqrt{(n+1)}\int {}^{n}\Psi_0(\boldsymbol{r}_2,\ldots,\boldsymbol{r}_{n+1})\ {}^{n+1}\Psi_x(\boldsymbol{r}_e,\boldsymbol{r}_2,\ldots,\boldsymbol{r}_{n+1}) \times\mathrm{d}\boldsymbol{r}_2\ldots\mathrm{d}\boldsymbol{r}_{n+1}, \tag{6}$$

where ${}^{n-1}\Psi_x$ and ${}^{n+1}\Psi_x$ denote the electronic wave functions of the xth ionized and electron-attached states, respectively; ${}^{n}\Psi_0$ denotes the electronic wave function of the neutral molecule; and $\phi_x^I(\boldsymbol{r}_h)$ and $\phi_x^E(\boldsymbol{r}_e)$ denote the DO corresponding to the ionized and electron-attached states, respectively. They can be easily obtained as expanded on the basis of the MOs (or in our case, the HOs) as

$$\phi_x^{\mathrm{I}}(\boldsymbol{r}) = \sum_i^{\mathrm{occ.}} \langle {}^{n}\Psi_0|\hat{i}^\dagger|{}^{n-1}\Psi_x\rangle\varphi_i(\boldsymbol{r}) = \sum_i^{\mathrm{occ.}} d_{x,i}^{\mathrm{I}}\varphi_i(\boldsymbol{r}), \tag{7}$$

$$\phi_x^{\mathrm{E}}(\boldsymbol{r}) = \sum_a^{\mathrm{virt.}} \langle {}^{n}\Psi_0|\hat{a}|{}^{n+1}\Psi_x\rangle\varphi_a(\boldsymbol{r}) = \sum_a^{\mathrm{virt.}} d_{x,a}^{\mathrm{E}}\varphi_a(\boldsymbol{r}), \tag{8}$$

where the $d_{x,i}^{\mathrm{I}}$ and $d_{x,a}^{\mathrm{E}}$ expansion coefficients are the *Dyson amplitudes*, which represent the contribution of each MO to the corresponding ionized and electron-attached states, respectively. An important property of DOs is that they do not form an orthogonal set, and the full set defined by Eqs. (5) and (6) can be linearly dependent.[24]

D. Construction of an effective Hamiltonian for NEGF

The principles of transport calculations using DFT-in-DFT embedding were described in our previous paper.[8] Following those ideas, in this paper, we present the generalization for correlated, many-electron methods.

In mean-field methods, the Koopmans picture[26] is applied to describe the ionized and electron-attached states by directly associating them with the molecular orbitals and the corresponding orbital energies, the Hamiltonian is thus simply given by the Fock matrix or the Kohn–Sham Hamiltonian. In contrast, within a many-electron framework, such a one-electron representation of the Hamiltonian is not inherently available. However, it can be constructed by using the IP and EA energies together with the corresponding DOs, where the Hamiltonian is considered diagonal with the electronic energies forming its diagonal elements. To incorporate such results into the NEGF framework, one needs to define a procedure for constructing an effective Hamiltonian matrix for the EM that is suitable for computing its Green's function [see Eq. (3)], required for evaluating the transmission function [see Eq. (2)]. For the molecule, the many-electron states obtained from the embedding calculation can be used to define an effective many-electron Hamiltonian in a spectral form as

$$\left({}^{HO}\mathbf{H}_M^{\mathrm{eff}}\right)_{pq} = -\sum_{x=1}^{N_I}\Delta E_x^{IP} d_{x,q}^{I}\left(d_{x,p}^{I}\right)^* - \sum_{x=1}^{N_E}\Delta E_x^{EA} d_{x,p}^{E}\left(d_{x,q}^{E}\right)^*, \tag{9}$$

where $d_{x,q}^{I/E}$ denotes the Dyson amplitudes of the many-electron ionized (I) and electron-attached (E) states in the basis of the HOs of the molecule, and ΔE_x^{IP} and ΔE_x^{EA} are the corresponding IPs and EAs, respectively. The left superscript explicitly denotes that this matrix is written in the basis of the HOs.

The construction of this matrix formally requires the knowledge of all possible many-electron states of the molecule. Because obtaining all such states is infeasible in practice, a Koopmans-type approximation can be applied for the states that are not explicitly determined at the correlated level, by using the HF HOs corresponding to the molecule, $\tilde{\mathbf{C}}_M$, and the respective orbital energies, $\tilde{\boldsymbol{\mathcal{E}}}_M$, obtained from the second SCF procedure (see Sec. II B). An effective Fock matrix for the complementary space of the DOs is built as

$$\tilde{\boldsymbol{\mathcal{H}}}_M^{\mathrm{Proj.}} = (\boldsymbol{I}-\mathbf{P}^{I,E})\tilde{\boldsymbol{\mathcal{E}}}_M(\boldsymbol{I}-\mathbf{P}^{I,E}) = \tilde{\boldsymbol{\mathcal{E}}}_M - \tilde{\boldsymbol{\mathcal{E}}}_M\mathbf{P}^{I,E} - \mathbf{P}^{I,E}\tilde{\boldsymbol{\mathcal{E}}}_M + \mathbf{P}^{I,E}\tilde{\boldsymbol{\mathcal{E}}}_M\mathbf{P}^{I,E}, \tag{10}$$

where $\mathbf{P}^{I,E}$ is a projector, which projects onto the space spanned by the determined many-electron states. This projector is defined as

$$\mathbf{P}_{pq}^{I,E} = \sum_{x,y=1}^{N_I}\left(\mathscr{S}^{-1}\right)_{xy} d_{x,q}^{I}\left(d_{y,p}^{I}\right)^* + \sum_{x,y=1}^{N_E}\left(\mathscr{S}^{-1}\right)_{xy} d_{x,p}^{E}\left(d_{y,q}^{E}\right)^*, \tag{11}$$

where $\mathscr{S}$ is the overlap matrix of the DOs, and N_I and N_E denote the number of ionized and electron-attached states explicitly determined, respectively. The effective Hamiltonian matrix for the molecule is then constructed by adding the projected HF Fock matrix to the many-electron effective Hamiltonian, Eq. (9), which is obtained only for a subset of many-electron states,

$${}^{HO}\mathbf{H}_M := {}^{HO}\mathbf{H}_M^{\mathrm{eff}} + \tilde{\boldsymbol{\mathcal{H}}}_M^{\mathrm{Proj.}}. \tag{12}$$

This approach effectively corrects the HF description of the embedded molecule within the energy window defined by the selected many-electron states. With the resulting effective Hamiltonian matrix, a mixed effective Hamiltonian matrix for the EM can be constructed. For the DFT-in-DFT embedding presented in Ref. 8, this step was performed in the AO basis: the molecular block of the supersystem Fock matrix ($\mathbf{F}_{EM}$) obtained in the first SCF step was replaced by the molecular block of the Fock matrix ($\tilde{\mathbf{F}}_{EM}$) of the second SCF step. Here, we use a slightly different procedure. Since the

molecular Hamiltonian ($^{HO}\mathbf{H}_M$) is available only in the HOs of the molecule, the supersystem Fock matrix ($\mathbf{F}_{EM}$) obtained in the first SCF step is transformed to the basis of the HOs,

$$^{HO}\mathbf{F}_{EM} = \tilde{\mathbf{C}}\,\mathbf{F}_{EM}\,\tilde{\mathbf{C}}^{\mathrm{T}}, \tag{13}$$

which allows the substitution of the effective Hamiltonian [Eq. (12)] into the block corresponding to the HOs of the molecule as follows:

$$^{HO}\mathbf{H}^{mix}_{EM} := \begin{pmatrix} ^{HO}\mathbf{H}_M & ^{HO}\mathbf{F}^{\mathrm{I}}_{El,M} \\ \left(^{HO}\mathbf{F}^{\mathrm{I}}_{El,M}\right)^{\mathrm{T}} & ^{HO}\mathbf{F}^{\mathrm{I}}_{El} \end{pmatrix}. \tag{14}$$

Finally, this effective Hamiltonian matrix is transformed back to the AO basis as

$$\mathbf{H}^{mix}_{EM} = \mathbf{S}_{EM}\,\tilde{\mathbf{C}}^{\mathrm{T}}\,^{HO}\mathbf{H}^{mix}_{EM}\,\tilde{\mathbf{C}}\,\mathbf{S}_{EM}, \tag{15}$$

which now can be used to construct the Green's function of the extended molecule using Eq. (3), enabling the calculation of the transmission function.

As introduced in Ref. 8 for the DFT-in-DFT case, the impact of the molecule on the orbitals of the EM can be characterized by the following quantity constructed from the overlap between individual supersystem MOs and the HOs of the embedded molecule,

$$\tilde{s}_p := \frac{1}{n_M}\sum_{q\in M}\left|\left(\tilde{\mathbf{C}}^{\mathrm{T}}_{EM}\,\mathbf{S}_{EM}\,\tilde{\mathbf{C}}_M\right)_{pq}\right|, \tag{16}$$

where n_M is the total number of the HOs of the molecule, p and q denote supersystem MOs and the HOs of the molecule, and $\tilde{\mathbf{C}}_{EM}$ and $\tilde{\mathbf{C}}_M$ contain the AO expansion of the eigenvectors of $\mathbf{H}^{mix}_{EM}$ and that of the HOs of the molecule, respectively. Thus, this number indicates the extent to which the orbitals of the molecule mix into a particular orbital of the EM.

III. COMPUTATIONAL DETAILS

Test calculations were performed for the systems investigated in Ref. 8. Details on obtaining the molecular structures and EM model systems are described in that work.[8] The aug-cc-pVDZ basis set was used on the atoms of the molecules, and the cc-pVDZ-PP basis set,[27] in combination with the def-PP-ECP effective core potential (ECP),[28] was applied for the gold atoms. The embedding calculations were performed with the MRCC program system,[29,30] where both arbitrary-level coupled-cluster models[31] and different variants of the ADC(2) method[32–35] are available as the high-level method in a WFT-in-DFT embedding. The recent, very efficient implementation of the latter model offers a direct calculation of ionized and electron-attached states by using linear response theory,[30] also producing the respective Dyson orbitals. With higher-level methods, such as CCSD, ionic states are currently accessible as electronic excitations using the continuum orbital technique,[36–39] with the DOs obtained as the block of the one-electron transition density matrix that corresponds to the continuum orbital.[40]

In addition to the WFT-in-DFT calculations, we have also performed DFT-in-DFT calculations with the above-described construction of the effective Hamiltonian using the MO basis. This way, the DFT-in-DFT and WFT-in-DFT calculations are directly comparable, and a comparison to the results of the slightly different, AO-based construction in Ref. 8 is possible as well. In the DFT-in-DFT calculations, the CAM-B3LYP functional was used. We note that, due to the presence of many unoccupied orbitals with negative orbital energy in the first supersystem DFT calculation, achieving convergence of the SCF procedure is generally not trivial, and the continuum molecular orbital has to be introduced only before the high-level subsystem calculation step. The core electrons were excluded from the correlation treatment in all WFT calculations presented here. The localization of the occupied space was performed using the SPADE approach,[19] while both the SPADE and PAO methods were applied for the virtual space, using a norm threshold of 0.3 (see Ref. 23 for details) for the latter. In the main text, the results obtained with the PAO localization are shown, whereas those based on the SPADE approach are presented in the supplementary material.

Calculation of the effective Hamiltonian [Eq. (12)] and the transmission functions [Eqs. (2) and (3)] was done with an in-house Python code,[41] with the lead self-energies sourced from periodic DFT calculations using Turbomole.[42] These calculations were also used to determine the Fermi level at −5.2 eV. Further details of the latter steps are given in Ref. 8.

IV. RESULTS AND DISCUSSION

A. Benchmarking wavefunction methods on molecular energy levels

A key requirement for a method to predict molecular conductance in a reliable way is an accurate description of molecular energy levels. In a many-electron framework, this can be benchmarked by inspecting the precision of the IP and EA values obtained for the isolated molecule, as well as for that in the junction using the embedding framework described above. Beyond the relative positioning of the IPs and EAs with respect to the Fermi energy of the leads, the energy gap between them also influences the molecular conductance, making its accurate prediction essential. To illustrate the failure of the commonly used PBE functional, the first IP and EA values obtained with different DFT functionals and the HF method were compared in our previous study.[8] Here, we extend this analysis by including the SOS-ADC(2) WFT method, which represents an attractive compromise between computational cost and accuracy, and is particularly well suited for predicting reliable IP and EA values.[38,43,44] As a reference, the EOM-CCSD(T) (a)* method[45] was chosen for the isolated BDA molecule, while EOM-CCSD calculations were performed for the substituted variants. The IP and EA values of the molecules were also determined in the extended molecule using the embedding framework with PBE-in-PBE, HF-in-PBE, and SOS-ADC(2)-in-PBE schemes. For comparison, CCSD-in-PBE results were additionally obtained for the BDA molecule in the extended molecule. Results are shown in Table I and S1–S4.

With the PBE functional, a significant underestimation of the IPs and overestimation of the EAs can be observed in all investigated cases. This results in a much smaller gap between the first IP and EA than in the reference case and even a wrong sign of the first EA. On the other hand, the HF and SOS-ADC(2) methods both show remarkably good performance for the selected molecules. With the HF method, the first IPs and EAs provided by Koopmans' theorem differ by no more than 0.2 to 0.6 eV and by −0.3 to −0.5 eV,

TABLE I. The first ionization potential (ΔE^{IP}) and electron affinity (ΔE^{EA}) values (in eV units) of the BDA, F_4-BDA, and Me_4-BDA molecules in isolation and within the junction, computed using the PBE functional for the electrodes in the embedding calculations.

Method	Isolated		Junction	
	ΔE_1^{IP}	ΔE_1^{EA}	ΔE_1^{IP}	ΔE_1^{EA}
BDA				
PBE[a]	4.28	0.99	6.78	1.32
HF[a]	7.32	−0.93	9.26	−0.28
SOS-ADC(2)	6.84	−0.73	8.62	−0.08
CCSD	7.09	−0.62	8.84	−0.02
CCSD(T) (a)*	7.12	−0.60		
F_4-BDA				
PBE[a]	4.92	1.55	6.81	1.54
HF[a]	8.28	−0.82	9.62	−0.35
SOS-ADC(2)	7.72	−0.52	8.93	−0.15
CCSD	7.87	−0.36		
Me_4-BDA				
PBE[a]	3.99	0.78	6.48	1.38
HF[a]	6.83	−0.91	8.86	−0.36
SOS-ADC(2)	6.49	−0.76	8.15	−0.14
CCSD	6.53	−0.51		

[a]Opposite of the corresponding molecular orbital energies.

respectively, from the reference values. However, a more pronounced discrepancy of ~1.4 eV relative to the reference is observed for the third IP with this method (see Table S1 in the supplementary material). While HF overestimates the IPs, SOS-ADC(2) underestimates them, but the difference is significantly smaller in the latter case, less than −0.15 eV. For the EAs, both methods result in underestimations, but the error is again consistently lower with SOS-ADC(2). Since HF overestimates the first IP while underestimating the first EA, the energy gap between these states is notably larger than in the reference. On the other hand, because the errors in SOS-ADC(2) are of the same sign, the resulting energy gap is more accurate, deviating by only −0.1 eV for BDA, by 0.2 eV for Me_4-BDA, and being nearly identical for F_4-BDA. The discrepancy increases for the higher IPs shown in Table S1, but this effect is also less significant with SOS-ADC(2), indicating that this method provides better approximations not only for the first IP but also for subsequent ones. However, for the EAs, no clear trend is observed, as the predictive accuracy for higher EAs remains similar to that of the first for both methods. These findings align with previous studies,[38] reinforcing that SOS-ADC(2) is an appropriate choice for use in the embedding scheme to compute molecular conductance. Moreover, also the HF model appears to be providing a reasonable description for the particular systems benchmarked here.

It is worth looking also at the relative position of the cationic and anionic energy levels with respect to the Fermi energy of the leads ($E_F = -5.2$ eV), as the energetically close-lying states are expected to influence the zero-bias conductance to the greatest extent. This should be investigated with the molecule embedded in the junction (see the last columns of Table I, as well as Tables S2 and S3). For BDA, the first IP with the HF method is 0.6 eV further from the Fermi energy compared to the SOS-ADC(2) result. A smaller, but opposite, deviation of −0.2 eV is found for the first EA, resulting in an energy gap between the first IP and EA wider by 0.8 eV in the HF case.

For the two substituted BDA variants, similar trends can be observed. When calculated using the HF method, the energy gap between the first IP and EA is larger for both F_4-BDA and Me_4-BDA than for BDA, yielding values of 10.0 and 9.2 eV, respectively. In contrast, the SOS-ADC(2) approach predicts a comparatively smaller gap for F_4-BDA (8.3 eV) and a slightly larger one for Me_4-BDA (9.0 eV), thereby restoring the expected trend among the three molecules. Nevertheless, compared to the PBE result, both models show a significant improvement for all investigated systems.

B. Transmission functions

Figure 1 presents the obtained transmission functions for the BDA SMJ with the supersystem PBE and the embedding approaches. Essentially, all embedding models yield very similar transmission curves. The agreement is particularly striking at the Fermi level and up to 1.4 eV above it, where the three curves are barely distinguishable. However, note the logarithmic scale of Fig. 1, which masks the minor differences in this region, amounting to more than 10 percent at E_F (see below). The general similarity of the curves can be explained by inspecting the spectrum of the embedded Hamiltonian [Eq. (15)] depicted on the bottom panel of Fig. 1, where the energy levels in all embedding approaches essentially align. The $\tilde{s}$ quantity, which characterizes the contribution of the molecule to the respective orbitals, also remains low, below 0.004 at all points. This shows that, in the vicinity of E_F, the spectrum (and thus, the conductance) is determined by orbitals of the electrodes, and the perturbation of the molecule on these levels is modest due to the large energetic separation of the nearest molecular levels (see Table I). However, around and below the Fermi level, the transmission functions provided by the embedding techniques lie noticeably below that of the conventional PBE approach, while above this point, they yield a transmission function exceeding the PBE result in most energy regions. In the former domain, the spectrum of $\mathbf{H}_{EM}^{mix}$ notably differs from that of the embedding models, and the $\tilde{s}$ overlaps are also significantly larger with PBE. The nearest PBE molecular orbitals, which lie closer in energy than in the WFT cases, thus mix more strongly with those of the electrodes, creating a larger conductance.

For the two substituted BDA variants shown in Figs. 2 and 3, very similar trends can be observed. As a result, the embedded approaches significantly reduce the value of the transmission function near the Fermi level compared to PBE. Furthermore, the relative properties of the HF-in-PBE and SOS-ADC(2)-in-PBE results remain remarkably consistent among all three BDA variants.

C. Zero-bias conductance

The zero-bias conductance values ($\mathscr{G}$) obtained with our embedding approaches, those from the conventional PBE method, and the GW many-electron approach,[46] as well as the corresponding

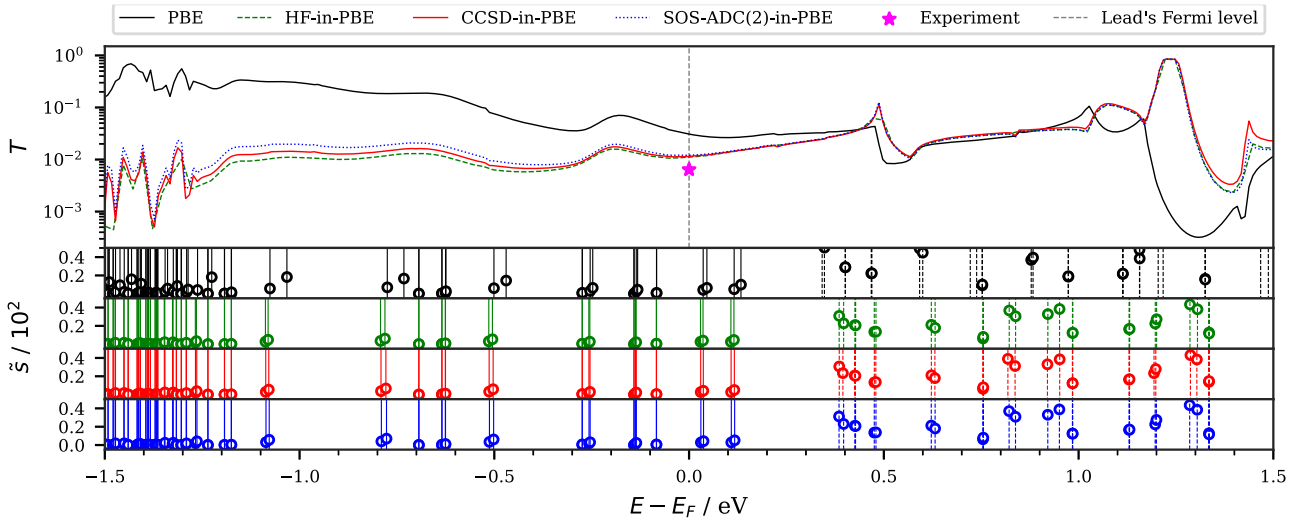

FIG. 1. Transmission functions (top panel) and eigenvalues of the embedded Hamiltonian [Eq. (14)] shown as vertical lines (solid for occupied and dashed for unoccupied levels), together with the corresponding $\tilde{s}$ values [Eq. (16)] indicated by circles (bottom panel) for the BDA SMJ using PBE (black), HF-in-PBE (green), SOS-ADC(2)-in-PBE (blue), and CCSD-in-PBE (red). Ten ionized and electron-attached states were included in the SOS-ADC(2)-in-PBE calculation, while five ionized and ten electron-attached states were considered in the CCSD-in-PBE case according to Eq. (12). The energy scale is shown relative to the Fermi level (−5.2 eV), indicated by a gray dashed line in the top panel.

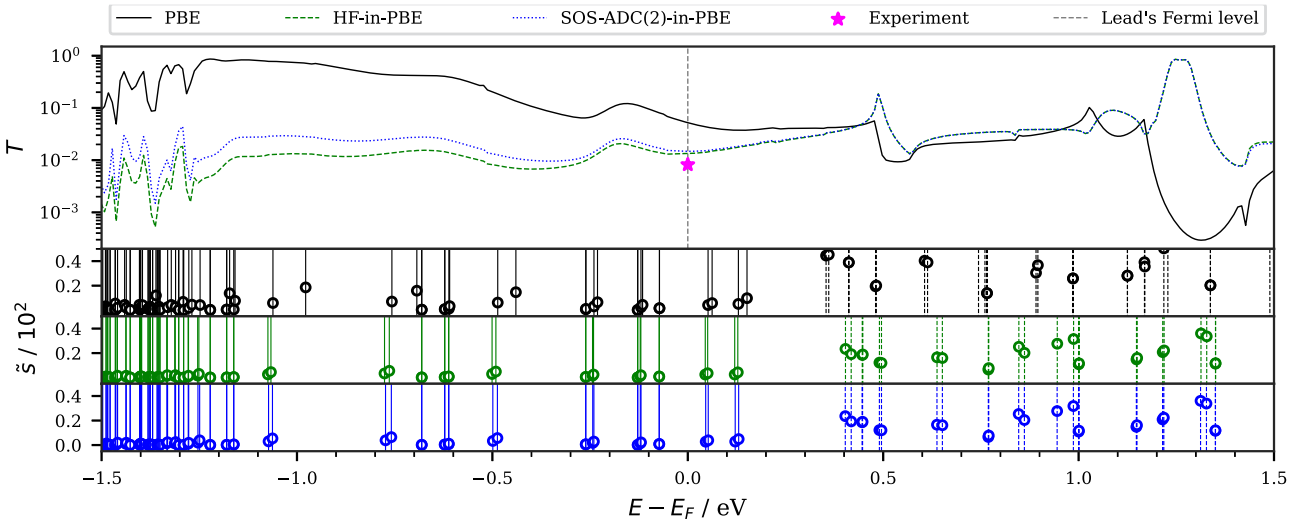

FIG. 2. Transmission functions (top panel) and eigenvalues of the embedded Hamiltonian [Eq. (14)] shown as vertical lines (solid for occupied and dashed for unoccupied levels), together with the corresponding $\tilde{s}$ values [Eq. (16)] indicated by circles (bottom panel) for the Me_4-BDA SMJ using PBE (black), HF-in-PBE (green), and SOS-ADC(2)-in-PBE (blue). Ten ionized and electron-attached states were included in the latter according to Eq. (12). The energy scale is shown relative to the Fermi level (−5.2 eV), indicated by a gray dashed line in the top panel.

experimental values for the BDA, F_4-BDA, and Me_4-BDA SMJs, are summarized in Table II. For all three SMJs, the embedding methods show consistently lower conductance compared to PBE and systematically overshoot the experimental values; however, the discrepancy is considerably smaller with the new methods. For all molecules, the HF method predicts slightly lower conductance values than the correlated methods, as well as the MO-based CAM-B3LYP, in accordance with the observation that HF tends to overestimate the energy gap between IPs and EAs. On the other hand, SOS-ADC(2) and CAM-B3LYP (MO) results are quite close in all cases. For BDA, the results obtained by these two latter methods deviate only modestly from CCSD. The sign of the deviation is the opposite of that of HF, indicating a possible overestimation of the effect of electron correlation.

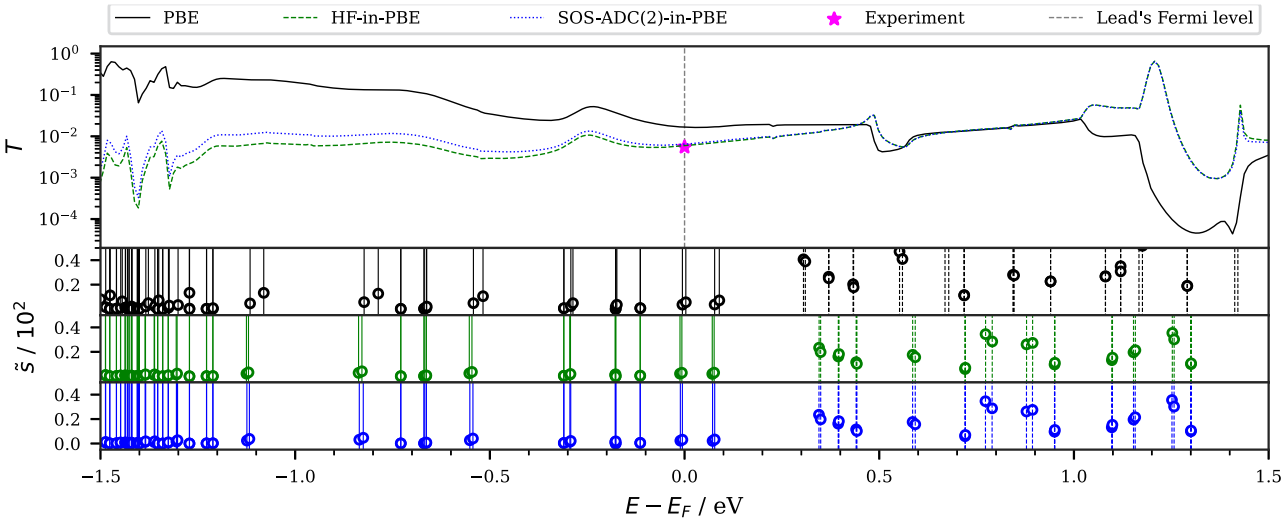

FIG. 3. Transmission functions (top panel) and eigenvalues of the embedded Hamiltonian [Eq. (14)] shown as vertical lines (solid for occupied and dashed for unoccupied levels), together with the corresponding $\tilde{s}$ values [Eq. (16)] indicated by circles (bottom panel) for the F_4-BDA SMJ using PBE (black), HF-in-PBE (green), and SOS-ADC(2)-in-PBE (blue). Ten ionized and electron-attached states were included in the latter according to Eq. (12). The energy scale is shown relative to the Fermi level (−5.2 eV), indicated by a gray dashed line in the top panel.

TABLE II. Calculated and experimental zero-bias conductances ($\mathscr{G}$) in units of $10^{-3}\,\mathscr{G}_0$ (=2 · 10^{-3} × 10^2/h).

	Me_4-BDA	BDA	F_4-BDA
Exp.[a]	8.2 ± 0.2	6.4 ± 0.2	5.5 ± 0.2
GW[b]	4.15	3.67	1.74
PBE	52.2	30.9	16.7
CAM-B3LYP-in-PBE[c] (AO)	15.8	5.3	2.8
CAM-B3LYP-in-PBE[c] (MO)	15.1	12.4	7.1
HF-in-PBE	13.3	11.1	5.9
SOS-ADC(2)-in-PBE	14.8	12.1	6.5
CCSD-in-PBE		11.6	

[a]Experimental values taken from Ref. 11.
[b]Values taken from Ref. 47.
[c]SPADE localization is used for the virtual space.

For comparison, the NEGF–GW results by Jin *et al.*[47] are also listed, as it represents another many-electron approach to this problem. With this method, a systematic underestimation of the experimental conductance values is observed, by factors of 1.7–3.2. In contrast, the same factors for the overestimation by the embedding methods are 1.1–1.7 for HF, 1.3–1.8 for CAM-B3LYP, and 1.2–1.8 for the SOS-ADC(2), showing a similar but somewhat smaller discrepancy than the GW method. The AO-based CAM-B3LYP-in-PBE variant, already introduced in Ref. 8, appears very accurate for BDA, but seems generally less systematic, because both over- and underestimation of the experiment are observed. The MO-based scheme shows a more consistent behavior with a systematic overestimation and an accuracy comparable to that of HF-in-PBE and SOS-ADC(2)-in-PBE.

As far as the computational demand is concerned, Thygesen and co-workers reported that a single GW self-consistency iteration for an SMJ containing the BDA molecule required about 2 h on 100–400 CPU cores, whereas the DFT calculation for the same system required no more than 5 h on eight CPU cores.[48] In contrast, for our model BDA SMJ, the PBE calculation took around 8 h using 12 CPU cores, while the complete SOS-ADC(2)-in-PBE procedure required ~26 h on the same system. In the latter case, the most time-consuming step is the transformation of the integrals from AO to HO basis after the second SCF step, which accounts for about 56% of the total runtime. Once this transformation is completed, the evaluation of the ionized states of the molecule with SOS-ADC(2) is practically negligible, taking less than 4 min for ten states, whereas the calculation of ten electron-attached states is more demanding but still relatively inexpensive, requiring about 1.5 h. Although our SMJ models contained smaller gold clusters, this comparison indicates that the use of embedding methods should not pose a prohibitive computational overhead once a supersystem DFT calculation is performed, which may not be the case with GW.

D. Impact of the number of Dyson orbitals in the embedding

The impact of the number of ionic states that are used in the WFT-in-DFT embedding approach [N_I and N_E in Eqs. (9) and (11)] on the convergence of the transmission function near the Fermi level is an important property that warrants investigation. For this purpose, the transmission functions were calculated for the BDA SMJ by applying the SOS-ADC(2)-in-PBE embedding approach, progressively including more states, from 1/1 to 10/10, with the number of ionized (N_I, first number) and electron-attached (N_E, second number) states increased equally. The energies of the employed states

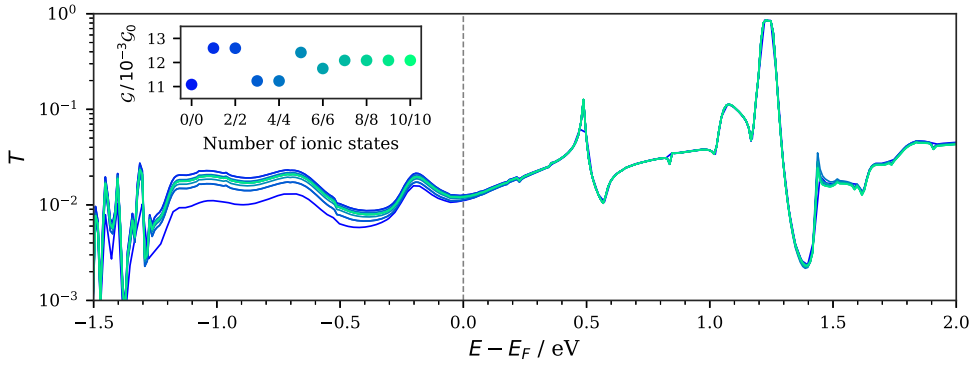

FIG. 4. SOS-ADC(2)-in-PBE transmission functions for the BDA SMJ using an increasing number of included ionic states from 0/0 to 10/10 by successively adding one ionized and one electron-attached state at each step. The corresponding zero-bias conductances are shown in the insets, using the same color scheme as the main plots. The energy scale is shown relative to the Fermi level (−5.2 eV), indicated by a gray dashed line in the top panel.

are listed in Table S4. The starting, non-correlated case (0/0) corresponds to the HF-in-PBE embedding, where no ionic states from the correlated method are included in Eq. (12). As the number of IP and EA states included from the SOS-ADC(2) calculation increases, the energy window around the Fermi level over which the molecular spectrum is adjusted becomes progressively wider. The resulting transmission functions, along with the corresponding zero-bias conductance values, are shown in Fig. 4. The results show that, while the inclusion of one ionized and one electron-attached state significantly alters the transmission function, the effect diminishes with each additional state. The effect is even negligible above the Fermi level as the transmission functions essentially coincide in all cases that include at least one ionized and electron-attached state. In contrast, below the Fermi level, the deviation of the transmission functions is significant. By the inclusion of the second ionized and electron-attached states, the transmission function remains almost unchanged across the entire energy range. However, with the addition of a third pair of states, a decrease in the transmission values is observed, and this trend does not continue with the inclusion of the fourth. Adding further ionic states causes the transmission function to increase slightly, but after the seventh pair, the transmission function does not show any further significant change. This means that, although the corresponding zero-bias conductance does not converge monotonically, it converges relatively quickly. When the number of included IP and EA states is increased separately (see Fig. S1), it is observed that the addition of the first, third, and fifth ionized states has the largest impact, whereas variations in the number of electron-attached states appear to have a smaller effect. These findings suggest that even a modest number of ionic states can be sufficient to accurately capture the necessary many-electron effects for describing electron transport near the Fermi level.

E. Role of the localization scheme

The convergence patterns observed above are remarkably insensitive to the choice of the orbital localization scheme used to produce the embedded subsystem space, as discussed in Sec. II B. Around and below the Fermi level, as shown in Fig. S2, the transmission functions obtained using different localization schemes exhibit only minimal differences, the values being slightly smaller when the PAO scheme is applied. We note nevertheless that the deviation of the SPADE and PAO results is significantly larger in the converged SOS-ADC(2) case than that observed with the HF (0/0) model. Above the Fermi level, the curves obtained with the two localization approaches differ considerably, and this effect is even more pronounced than that of the chosen electronic structure method for the molecule. This finding confirms that the SPADE algorithm produces an improper subsystem virtual space[21,23] and, thus, inaccurately described electron-attached states, which impacts the resulting transmission curves as well. This is in contrast with the behavior of DFT-in-DFT embedding observed previously,[8] which is not surprising as the quality of the subsystem virtual space primarily impacts correlated models that involve excited determinants in their wave function. Thus, the use of the PAO method in such correlated WFT-in-DFT conductance calculations appears to be of paramount importance.

V. SUMMARY AND CONCLUSION

In this work, a novel approach to molecular conductance calculations using WFT-in-DFT projection-based embedding was introduced, which uses Dyson orbitals to incorporate many-body effects into the commonly used NEGF framework. The principal advantage of this approach lies in its ability to use sophisticated *ab initio* correlated methods for the embedded subsystem, offering a systematic way to improve the treatment of electron correlation in the molecular region. This avoids inheriting the deficiencies of a DFT reference, as the many-electron description of the molecule is obtained independently. This eliminates the need for any *ad hoc* empirical tuning parameters in transport calculations, such as artificially shifting the molecular spectrum, which are often used[6,7,12,49,50] to compensate for the deficiencies of the DFT functional in the description of the molecular domain. Formally, any WFT method capable of computing ionic states–either directly or as excited states via the continuum orbital technique–can be employed within the proposed framework. For small molecules, even expensive many-electron models high in the hierarchy of Coupled Cluster methods can be feasible, offering superior accuracy for computing the required ionic states. Nevertheless, given the growing interest in large organic molecules as potential components in molecular electronics, more affordable approximations are required to maintain computational feasibility. For this reason, the SOS-ADC(2) method was suggested as a reasonable candidate, as it strikes a favorable balance between computational cost and accuracy. The resulting transport

calculations with the embedding scheme yielded a significant improvement in the predicted zero-bias conductance compared to conventional NEGF–DFT results obtained using the PBE functional throughout the entire system. We showed that the observed improvement was primarily due to the shift in molecular energy levels, which increases the gap between the first IP and EA. This leads to a weaker mixing between molecular and electrode states, thereby reducing the transmission and correcting the overestimation of conductance observed with the PBE-based approach. The proposed scheme, using the SOS-ADC(2) model as the high-level method in the embedding, provided an accuracy comparable to the NEGF–GW scheme proposed by Thygesen and co-workers.[47,48,51] In the observed examples, even the much simpler HF-in-DFT embedding model showed a good performance, which is because Koopmans' theorem provides a relatively accurate estimation of the IPs and EAs in these cases, even for the molecule embedded in the junction. However, this should not be expected as a general behavior, and we strongly advocate the use of a correlated model for the embedded subsystem. Doing so should not pose a computational limitation, as the high-level calculations are performed solely for the molecule, and the SOS-ADC(2) technique proposed above possesses a fourth-order scaling with the system size, making the calculation of several ionic states accessible at a very modest computational cost. Nevertheless, the embedding framework has the flexibility that allows it to always adopt the most appropriate electronic structure method for the molecular domain, and the accuracy of the predicted IPs and EAs for the isolated or embedded molecules provides a reliable indicator of the performance of a given method in transport calculations.

SUPPLEMENTARY MATERIAL

The supplementary material supplied with this article presents the IP and EA values of the molecules in isolation and within the junction, calculated at different levels in Tables S1–S4. The comparison of transmission functions obtained with different virtual-space localization schemes and with varying numbers of included ionic states is presented in Figs. S1–S2.

ACKNOWLEDGMENTS

This work has been supported by the National Research, Innovation and Development Fund (NKFIA) of Hungary (Grant No. 142634). D.P.J. acknowledges the support by the EKÖP-24 University Excellence Scholarship Programme of the Ministry for Culture and Innovation from the source of the National Research, Development and Innovation Fund. D.M. acknowledges the János Bolyai Research Scholarship of the Hungarian Academy of Sciences. The authors thank Dr. Bence Hégely, Professor Mihály Kállay, and Dr. László Oroszlány for useful discussions. The authors appreciate the computational resources provided by the ELTE IIG High-Performance Computing facility.

AUTHOR DECLARATIONS

Conflict of Interest

The authors have no conflicts to disclose.

Author Contributions

Dávid P. Jelenfi: Conceptualization (equal); Data curation (lead); Formal analysis (lead); Investigation (lead); Methodology (lead); Software (lead); Validation (lead); Visualization (lead); Writing – original draft (equal); Writing – review & editing (supporting). **Dávid Mester**: Software (supporting); Writing – review & editing (equal). **Attila Tajti**: Conceptualization (equal); Formal analysis (supporting); Funding acquisition (supporting); Investigation (supporting); Methodology (equal); Project administration (supporting); Supervision (equal); Validation (supporting); Writing – original draft (equal); Writing – review & editing (lead). **Péter G. Szalay**: Conceptualization (equal); Formal analysis (equal); Funding acquisition (lead); Investigation (supporting); Methodology (supporting); Project administration (lead); Supervision (equal); Writing – original draft (supporting); Writing – review & editing (supporting).

DATA AVAILABILITY

The data that support the findings of this study are available within the article and its supplementary material.

REFERENCES

[1] P. Gehring, J. M. Thijssen, and H. S. J. van der Zant, "Single-molecule quantum-transport phenomena in break junctions," Nat. Rev. Phys. **1**, 381–396 (2019).
[2] P. T. Mathew and F. Fang, "Advances in molecular electronics: A brief review," Engineering **4**, 760–771 (2018).
[3] M. Brandbyge, J.-L. Mozos, P. Ordejón, J. Taylor, and K. Stokbro, "Density-functional method for nonequilibrium electron transport," Phys. Rev. B **65**, 165401 (2002).
[4] Y. Xue, S. Datta, and M. A. Ratner, "First-principles based matrix Green's function approach to molecular electronic devices: General formalism," Chem. Phys. **281**, 151–170 (2002).
[5] J. P. Perdew, K. Burke, and M. Ernzerhof, "Generalized gradient approximation made simple," Phys. Rev. Lett. **77**, 3865–3868 (1996).
[6] S. Y. Quek, L. Venkataraman, H. J. Choi, S. G. Louie, M. S. Hybertsen, and J. B. Neaton, "Amine-gold linked single-molecule circuits: Experiment and theory," Nano Lett. **11**, 3477 (2007).
[7] J. A. Celis Gil and J. M. Thijssen, "Transport gap renormalization at a metal-molecule interface using DFT-NEGF and spin unrestricted calculations," J. Chem. Phys. **147**, 084102 (2017).
[8] D. P. Jelenfi, A. Tajti, and P. G. Szalay, "Molecular conductance calculations of single-molecule junctions using projection-based density functional embedding," Chem. Phys. **162**, 034101 (2025).
[9] B. Hégely, P. R. Nagy, G. G. Ferenczy, and M. Kállay, "Exact density functional and wave function embedding schemes based on orbital localization," J. Chem. Phys. **145**, 064107 (2016).
[10] L. Venkataraman, J. E. Klare, C. Nuckolls, M. S. Hybertsen, and M. L. Steigerwald, "Dependence of single-molecule junction conductance on molecular conformation," Nature **442**, 904 (2006).
[11] L. Venkataraman, Y. S. Park, A. C. Whalley, C. Nuckolls, M. S. Hybertsen, and M. L. Steigerwald, "Electronics and chemistry: Varying single-molecule junction conductance using chemical substituents," Nano Lett. **7**, 502–506 (2007).
[12] M. Dell'Angela, G. Kladnik, A. Cossaro, A. Verdini, M. Kamenetska, I. Tamblyn, S. Y. Quek, J. B. Neaton, D. Cvetko, and A. V. L. Morgante, "Relating energy level alignment and amine-linked single molecule junction conductance," Nano Lett. **10**, 2470 (2010).
[13] R. Landauer, "Conductance determined by transmission: Probes and quantised constriction resistance," J. Phys. Condens. Matter **1**, 8099 (1989).
[14] J. Taylor, H. Guo, and J. Wang, "Ab initio modeling of quantum transport properties of molecular electronic devices," Phys. Rev. B **63**, 245407 (2001).

[15]Y. Meir and N. S. Wingreen, "Landauer formula for the current through an interacting electron region," Phys. Rev. Lett. **68**, 2512 (1992).
[16]L. Keldysh, "Diagram technique for nonequilibrium processes," Zh. Ekps. Teor. Fiz. **47**, 1515 (1964).
[17]M. Thoss and F. Evers, "Perspective: Theory of quantum transport in molecular junctions," J. Chem. Phys. **148**, 030901 (2018).
[18]S. Huzinaga and A. A. Cantu, "Theory of separability of many-electron systems," J. Chem. Phys. **55**, 5543–5549 (1971).
[19]D. Claudino and N. J. Mayhall, "Automatic partition of orbital spaces based on singular value decomposition in the context of embedding theories," J. Chem. Theory Comput. **15**, 1053–1064 (2019).
[20]B. Barcza, Á. B. Szirmai, A. Tajti, J. F. Stanton, and P. G. Szalay, "Benchmarking aspects of ab initio fragment models for accurate excimer potential energy surfaces," J. Chem. Theory Comput. **19**, 3580–3600 (2023).
[21]Á. B. Szirmai, B. Hégely, A. Tajti, M. Kállay, and P. G. Szalay, "Projected atomic orbitals as optimal virtual space for excited state projection-based embedding calculations," J. Chem. Theory Comput. **20**, 3420–3425 (2024).
[22]J. W. Boughton and P. Pulay, "Comparison of the boys and Pipek–Mezey localizations in the local correlation approach and automatic virtual basis selection," J. Comput. Chem. **14**, 736–740 (1993).
[23]Á. B. Szirmai, B. Bónis, A. Tajti, and P. G. Szalay, "Accuracy of projected atomic virtual orbital space in embedding applications," Mol. Phys. **122**, e2355694 (2024).
[24]O. Goscinski and P. Lindner, "Natural spin-orbitals and generalized overlap amplitudes," J. Math. Phys. **11**, 1313–1317 (1970).
[25]J. V. Ortiz, "Dyson-orbital concepts for description of electrons in molecules," J. Chem. Phys. **153**, 070902 (2020).
[26]T. Koopmans, "Über die zuordnung von wellenfunktionen und eigenwerten zu den einzelnen elektronen eines atoms," Physica **1**, 104–113 (1934).
[27]K. A. Peterson and C. Puzzarini, "Systematically convergent basis sets for transition metals. II. Pseudopotential-based correlation consistent basis sets for the group 11 (Cu, Ag, Au) and 12 (Zn, Cd, Hg) elements," Theor. Chem. Acc. **114**, 283–296 (2005).
[28]D. Figgen, G. Rauhut, M. Dolg, and H. Stoll, "Energy-consistent pseudopotentials for group 11 and 12 atoms: Adjustment to multi-configuration Dirac–Hartree–Fock data," Chem. Phys. **311**, 227–244 (2005).
[29]M. Kállay, P. R. Nagy, D. Mester, Z. Rolik, G. Samu, J. Csontos, J. Csóka, P. B. Szabó, L. Gyevi-Nagy, B. Hégely, I. Ladjánszki, L. Szegedy, B. Ladóczki, K. Petrov, M. Farkas, P. D. Mezei, and Á. Ganyecz, "The MRCC program system: Accurate quantum chemistry from water to proteins," J. Chem. Phys. **152**, 074107 (2020).
[30]D. Mester, P. R. Nagy, J. Csóka, L. Gyevi-Nagy, P. B. Szabó, R. A. Horváth, K. Petrov, B. Hégely, B. Ladóczki, G. Samu, B. D. Lőrincz, and M. Kállay, "Overview of developments in the MRCC program system," J. Phys. Chem. A **129**, 2086–2107 (2025).
[31]M. Kállay and J. Gauss, "Calculation of excited-state properties using general coupled-cluster and configuration-interaction models," J. Chem. Phys. **121**, 9257–9269 (2004).
[32]J. Schirmer, "Beyond the random-phase approximation: A new approximation scheme for the polarization propagator," Phys. Rev. A **26**, 2395–2416 (1982).
[33]A. Hellweg, S. A. Grün, and C. Hättig, "Benchmarking the performance of spin-component scaled CC2 in ground and electronically excited states," Phys. Chem. Chem. Phys. **10**, 4119–4127 (2008).
[34]N. O. C. Winter and C. Hättig, "Scaled opposite-spin CC2 for ground and excited states with fourth order scaling computational costs," J. Chem. Phys. **134**, 184101 (2011).
[35]D. Mester, P. R. Nagy, and M. Kállay, "Reduced-cost second-order algebraic-diagrammatic construction method for excitation energies and transition moments," J. Chem. Phys. **148**, 094111 (2018).
[36]M. Nooijen and R. J. Bartlett, "Similarity transformed equation-of-motion coupled-cluster theory: Details, examples, and comparisons," J. Chem. Phys. **107**, 6812–6830 (1997).
[37]J. F. Stanton and J. Gauss, "A simple scheme for the direct calculation of ionization potentials with coupled-cluster theory that exploits established excitation energy methods," J. Chem. Phys. **111**, 8785–8788 (1999).
[38]A. Shaalan Alag, D. P. Jelenfi, A. Tajti, and P. G. Szalay, "Accurate prediction of vertical ionization potentials and electron affinities from spin-component scaled CC2 and ADC(2) models," J. Chem. Theory Comput. **18**, 6794–6801 (2022).
[39]D. P. Jelenfi, A. Tajti, and P. G. Szalay, "First-principles interpretation of electron transport through single-molecule junctions using molecular dynamics of electron attached states," Mol. Phys. **119**, e1999518 (2021).
[40]C. Melania Oana and A. I. Krylov, "Dyson orbitals for ionization from the ground and electronically excited states within equation-of-motion coupled-cluster formalism: Theory, implementation, and examples," J. Chem. Phys. **127**, 234106 (2007).
[41]D. P. Jelenfi (2025). "A NEGF-embedding transport code," GitHub. https://github.com/JelenDP/Transport_Code
[42]S. G. Balasubramani, G. P. Chen, S. Coriani, M. Diedenhofen, M. S. Frank, Y. J. Franzke, F. Furche, R. Grotjahn, M. E. Harding, C. Hättig, A. Hellweg, B. Helmich-Paris, C. Holzer, U. Huniar, M. Kaupp, A. Marefat Khah, S. Karbalaei Khani, T. Müller, F. Mack, B. D. Nguyen, S. M. Parker, E. Perlt, D. Rappoport, K. Reiter, S. Roy, M. Rückert, G. Schmitz, M. Sierka, E. Tapavicza, D. P. Tew, C. van Wüllen, V. K. Voora, F. Weigend, A. Wodyński, and J. M. Yu, "TURBOMOLE: Modular program suite for ab initio quantum-chemical and condensed-matter simulations," J. Chem. Phys. **152**, 184107 (2020).
[43]A. Tajti, L. Tulipán, and P. G. Szalay, "Accuracy of spin-component scaled ADC(2) excitation energies and potential energy surfaces," J. Chem. Theory Comput. **16**, 468–474 (2020).
[44]D. Mester and M. Kállay, "Vertical ionization potentials and electron affinities at the double-hybrid density functional level," J. Chem. Theory Comput. **19**, 3982–3995 (2023).
[45]D. A. Matthews and J. F. Stanton, "A new approach to approximate equation-of-motion coupled cluster with triple excitations," J. Chem. Phys. **145**, 124102 (2016).
[46]F. Aryasetiawan and O. Gunnarsson, "The *GW* method," Rep. Prog. Phys. **61**, 237 (1998).
[47]C. Jin, M. Strange, T. Markussen, G. C. Solomon, and K. S. Thygesen, "Energy level alignment and quantum conductance of functionalized metal-molecule junctions: Density functional theory versus GW calculations," J. Chem. Phys. **139**, 184307 (2013).
[48]M. Strange, C. Rostgaard, H. Häkkinen, and K. S. Thygesen, "Self-consistent gw calculations of electronic transport in thiol-and amine-linked molecular junctions," Phys. Rev. B **83**, 115108 (2011).
[49]D. J. Mowbray, G. Jones, and K. S. Thygesen, "Influence of groups on charge transport in molecular junctions," J. Chem. Phys. **128**, 111103 (2008).
[50]S. Y. Quek, H. J. Choi, S. G. Louie, and J. B. Neaton, "Length dependence of conductance in aromatic single-molecule junctions," Nano Lett. **9**, 3949–3953 (2009).
[51]K. S. Thygesen and A. Rubio, "Conserving *GW* scheme for nonequilibrium quantum transport in molecular contacts," Phys. Rev. B **77**, 115333 (2008).